

Biosynthesis of 3D/2D Ceo₂/Mos₂ Nanocomposites with Enhanced Photocatalytic Activity to Degrade Organic Dye in Wastewater and Statistical Optimization of Reaction Parameters

Yogesh Sharma

Vellore Institute of Technology

Mohammad Ahmed Khan

Vellore Institute of Technology

Thangapandi Chellapandi

Vellore Institute of Technology

Magdum Tejas Sukumar

Vellore Institute of Technology

Gunabalan Madhumitha

Vellore Institute of Technology

Md. Maksudur Rahman Khan

University Malaysia Pahang

Mohammed Danish

Universi Sains Malaysia

Sagadevan Velu

Vellore Institute of Technology

Selvaraj Mohana Roopan (✉ mohanarooan.s@vit.ac.in)

Vellore Institute of Technology <https://orcid.org/0000-0002-5610-7443>

Research Article

Keywords: Biosynthetic method, Methyl Violet, Nanocomposites, Optimization, Photocatalyst, Visible light

Posted Date: September 1st, 2021

DOI: <https://doi.org/10.21203/rs.3.rs-853778/v1>

License:   This work is licensed under a Creative Commons Attribution 4.0 International License.

[Read Full License](#)

Abstract

Nanocomposites synthesized by alternative approaches like biosynthetic methods are safer than those prepared by traditional chemical techniques. Further, this approach is both economically and environmentally feasible. In this study, we report an eco-friendly methodology for preparing cerium dioxide/molybdenum disulphide ($\text{CeO}_2/\text{MoS}_2$) nanocomposites. *Moringa oleifera* peel was used as the reducing/stabilizing agent for synthesizing CeO_2 nanoparticles. The prepared nanocomposites were characterized using FT-IR analysis, SEM and EDAX analysis, TEM and SAED pattern analysis, X-Ray Diffraction Pattern, Zeta Potential, UV-Visible Diffuse Reflectance Spectra, X-Ray Photon Spectroscopy and Photoluminescence spectra. Particle size and morphology were characterized by TEM and SEM. The photocatalytic pursuit of $\text{CeO}_2/\text{MoS}_2$ was explored by the degradation of methyl violet (MV) under visible light irradiation. Our methodology proved to be 96.25% effective in the degradation of MV. Further, we used this Response Surface Methodology for enhancing the process factors like volume of photocatalyst, time for degradation and concentration of MV.

Introduction

Persistent organic pollutants may cause chronic toxicity, which can be potentially carcinogenic and teratogenic [1]. Treatment of organic pollutants in wastewater is an urgent requirement and has drawn extensive attention because of its degradation resistance due to chemical stability [2]. The most common organic pollutants are derivatives of benzene, phenols, halogenated hydrocarbons, and organic dyes [1, 3]. These organic molecules are highly toxic and are chemically stable which facilitates their entry into the food chain [4] via aquatic organisms [5]. For the disposal of organic pollutants, many technologies such as biodegradation [6], adsorption [7], ultra-filtration, electrochemical, photochemical, chemical oxidation, electrochemical combustion [8] and other conventional techniques [9] have been used in recent past. The photocatalytic technique is an advanced oxidation process (AOP) that has been effectively used for the treatment of organic pollutants in water bodies. The advantages of this widely accepted technique are that it is cost-efficient, environment friendly and is highly efficient [10].

Photoactive materials facilitate the use of renewable source of energy (from solar light) to provide more effective and cleaner removal of organic pollutants. Extensive studies have been conducted in recent past on various compounds such as TiO_2 [11–13], CdS [14], ZnO [15, 16], SnO_2 [17], $\alpha\text{-Fe}_2\text{O}_3$ [18], Fe_3O_4 [19], $\text{g-C}_3\text{N}_4$ [20] and BiVO_4 [21] which have excellent performance as photocatalysts. Several two-dimensional (2D) materials such as graphitic carbon nitrile and graphene have been the centre of attraction for many years [20]. Low bandgap for AOP and antibacterial activity makes 2D materials perfect binding agents for wastewater treatment applications. Recent studies have introduced a 2D structure, molybdenum disulphide (MoS_2) which has attracted significant heed in the area of photocatalytic degradation [22], catalysis [23], photonics, energy technology [24], material sciences, biosensors [25] and micro-electronics [26]. Good biocompatibility and low toxicity are major factors for the increased use of MoS_2 in environmental applications. Due to the layered structure of MoS_2 , it possesses a large surface area,

suitable band gaps, chemically inertness, lubrication, catalysis, and anisotropy. Although, MoS₂ has been used as photocatalyst [27–30], high recombination rate with narrow band gap of the electron-hole pair restrict its photocatalytic activity. Rare earth oxides of ceria are a widely accepted photocatalyst and has been researched for a long time [31]. Cerium Oxide (CeO₂) nanoparticles can be synthesized in multiple ways, which primarily includes electrochemical [32], chemical reduction [33], microemulsion [34], microwave [35], and hydrothermal [36, 37], etc. Some of these methods uses carcinogenic chemical compounds and have complex reaction conditions. CeO₂ seems to be a promising candidate like TiO₂ and ZnO as it has desired properties such as non-toxicity, enhanced chemical stability, cost efficiency and easy synthesis. Although CeO₂ has been a good supporter for catalyst [38], it has some drawbacks as a photocatalyst due to limited light absorption ability, wide band gap, and a higher rate of recombination [39]. As mentioned earlier, CeO₂ is a good supporter of catalyst [38]. Therefore, CeO₂ can be an ideal candidate for combining with MoS₂ because of its larger surface area, proper band edge and suitable lattice match [40–44].

In the present study, we report the preparation (first-time) of CeO₂/MoS₂ composites with the help of methanolic peel extract of the *Moringa oleifera* (*M. oleifera*). Various characterization techniques examined the parameters affecting the structure and morphology of the nanocomposites. Photocatalytic activity of the CeO₂/MoS₂ nanocomposites has been determined using organic pollutants such as methyl violet. Response Surface Methodology was applied to optimize the process parameters like amount of photocatalyst, time for degradation, and concentration of MV dye [45, 46].

Experimental

Materials and Methods

M. oleifera was procured from Vellore Market, Vellore, Tamil Nadu, India. Botanical Survey of India, Coimbatore performed the peel authentication (BSI/SRC/S/23/2013–14/tech.1116). Thiourea, tartaric acid, ethanol, sodium hydroxide, ceric ammonium nitrate, ammonium molybdate, hydrazine hydrate, methyl violet, and aqueous ammonia were purchased from Sigma Aldrich, India. Analytical grade chemicals were utilized as received without any prior treatment. The solutions were prepared using Milli-Q water.

Peel extract preparation of *M. oleifera*

M. oleifera was collected from marketplace in Vellore, Tamil Nadu, India. The peel separation was performed using the traditional method i.e., peels of drumstick was collected and processed [35]. The peel of *M. oleifera* was detached from the drumsticks. This peel was cleaned using distilled water numerous times and then powdered using an electrical grinder. In accordance with the maceration protocol, 100 g of dried powder was treated with 500 mL methanol in a glass beaker. Distillation under controlled

temperature was done to concentrate the solvent to a syrupy viscosity. This extract was used as a stabilizing agent for the preparation of CeO₂ nanoparticles.

Green synthesis of CeO₂ nanoparticles

The protocol was followed as per the earlier report with little modification [35]. Ceric ammonium nitrate solution of 0.1 M was prepared and kept on magnetic stirrer. Methanolic *M. oleifera* peel extract was subjected. dropwise in the ceric ammonium nitrate solution until a pH in the preferable range of 8 to 9 was obtained. The colour of the solution turned light yellow. This solution was kept in the microwave at 300 W power, 60 °C for 15 min. The CeO₂ particulates formed visibly and were left to settle. After some time, these particulates were washed with water and ethanol. The washing of CeO₂ particles was essential to remove organic and inorganic impurities. Water removes the inorganic impurities such as unreacted ceric ammonium nitrate, whereas ethanol removes the organic impurities which might form during the working of the microwave. Washing with water also helps in achieving the desired pH. After washing the CeO₂ particulates, it was centrifuged at 4000 rpm and dried using a vacuum oven at 60 °C for 3 h. This dried product obtained was crushed and kept in a muffle furnace at 450 °C for 3 h. This process is known as calcination. The dried product obtained was Cerium oxide (CeO₂), which was greenish-yellow in colour.

Synthesis of 2D MoS₂ sheet

Synthesis of MoS₂ nanosheets were conducted by following the method reported by Gradkar et al. [47]. Experimental details of “Synthesis of 2D MoS₂ sheet” are presented in Supplementary Information (SI).

Preparation of composites

Composites of CeO₂/MoS₂ were prepared by fixing mass of CeO₂ at 300 mg and MoS₂ mass was varied at 2, 4, 6, and 8% (of 300 mg). MoS₂ and CeO₂ were weighed and added in 50 mL distilled water. This mixture of composites was stirred on a magnetic stirrer for about 30 min. After stirring, ultra-sonication was done at 300 W power, 27000 frequency for 15 min. Mixtures were separated and centrifuged at 6000 rpm. After centrifugation the sample was kept dry for 24 h at 60 °C. The dried product so obtained was CeO₂/MoS₂ composite. Ratio of composite composition was tabled below.

Characterization

The absorbance was recorded using UV–Visible spectroscopy Hitachi U2910. Functional groups present were examined using FT-IR spectroscopy SHIMAZDU infrared spectrophotometer (4000 to 400 cm⁻¹;

resolution: 1 cm^{-1}). KBr was used in the ratio of 1:100 (sample to KBr weight ratio) to prepare solid thin film. The crystallinity was analysed using Power XRD, Bruker (Germany, model D8). The XRD data was recorded for 2θ values lying in the range of 10 to 90 degrees. TEM and SAED pattern were recorded on TEM Philips CM-200 with operating voltage of 20-200 kV and 2.4 \AA resolution. Surface morphology was analysed on SEM/EDX (JEOL Model JSM - 6390LV). Zeta potential was analysed on Horiba Nanoparticle Analyzer (Model No. SZ 100). The XPS was computed using Physical Electronics equipment with model no. PHI 5000 Versa Probe III. The signal of C 1s was put at 285.2 eV.

Photocatalytic degradation

Experiments involving photocatalytic degradation were carried out in a Haber multi-lamp photochemical reactor. This photochemical reactor can provide a visible light source at 300 W using a cut-off filter in order to eliminate undesirable wavelengths ($<420 \text{ nm}$), to make sure that only visible light is used during irradiation. Decomposition of the MV dye in the existence of visible light proved efficiency of the $\text{CeO}_2/\text{MoS}_2$ nanocomposites in photocatalysis. 20 mg of the nanocomposite samples were transferred to 100 ml solution of MV dye at a concentration of 20 mg/L to study the photodegradation efficiency of nanocomposites. The suspension was stirred in darkness to achieve an equilibrium of sorption-desorption for 30 min. Thereafter, the solutions were irradiated with a visible lamp and the temperature kept constant at $25 \text{ }^\circ\text{C}$. The solution samples were collected after every 15 min and kept in dark. The concentrations of MV were monitored by measuring the absorbance against the wavelength *via* UV-vis spectrometer to record maximum absorbance wavelength (λ_{max}). With the decrease of concentration, the peak height decreased.

Central composite design (CCD)

RSM is an analysis which combines both statistical and mathematical techniques for optimizing, developing, and improving a process and allows to determine and evaluate the relative significance and interaction of all variables used. The experiment is especially designed for optimization of affective variables to enhance characteristics performance and reduce the experimental errors [48–51]. Important variables are selected using minimum number of trial runs. Three variables were used for making the CCD which are- the amount of photocatalyst, time for degradation, and concentration of MV dye. The relation between the independent variables were estimated as:

$$Y = \beta_0 + \sum_{i=1}^3 \beta_i X_i + \sum_{i=1}^3 \sum_{j=1}^3 \beta_{ij} X_i X_j + \sum_{i=1}^3 \beta_{ii} X_i^2$$

Where y denotes the degradation percentage of MV (response), $X_i X_j$ denotes the independent variables. The linear coefficient is β_i , β_0 is constant for the model and the quadratic coefficients are β_{ii} , β_{ij} . They are the cross-product coefficients. MV dye concentration of 10.0–30.0 mg/L has been selected. The amount

of photocatalyst was in the range of 10 to 30 mg and time was in the range of 75 to 105 min. CCD was used to evaluate the required number of runs for the experiments. The number of iterations used were 20.

In this investigation, the CCD of 3 factors with 4 central points were considered. The alpha axial value was picked as rotatable alpha 6.0 and the levels of the factors were determined as axial points (inscribed). One replicate was used with one response.

Results And Discussion

X-Ray Diffraction Pattern (XRD)

The powder X-ray diffraction was conducted to study the crystalline structure, phase, purity, and composition of the synthesised nanocomposites. The XRD patterns of CeO_2 , MoS_2 , and $\text{CeO}_2/\text{MoS}_2$ nanocomposites are illustrated in Fig. 1. The peaks at 2θ value of 28.44, 33.05, 47.46, 56.4, 58.75, 69.37, 76.73 and 79.18° represent the planes (110), (200), (220), (311), (222), (400), (331) and (420) respectively. The diffraction pattern revealed the cubic structure of CeO_2 which was in understanding with JCPDS 34-0394 [52]. The distinctive peaks displayed by MoS_2 sheet representing the (002), (100), (103) and (110) planes reveal the hexagonal structure of MoS_2 , which agrees with JCPDS 37-1492 [53]. No other prominent peak implies high purity and good crystallinity of the sample.

MoS_2 nanosheets comprised of 2D structure which were amorphous in nature, whereas CeO_2 nanoparticles which had 3D structure were crystalline in nature (Fig. 1- MS and C). Despite of this, MoS_2 characteristic patterns were not obtained in the XRD pattern of $\text{CeO}_2/\text{MoS}_2$ nanocomposites. The reason for this could be the effective intercalation of CeO_2 on MoS_2 sheets in the $\text{CeO}_2/\text{MoS}_2$ photocatalyst. It was observed that after the introduction of CeO_2 , the peaks at 2θ angle of 28.81, 33.48, 47.9, 56.84, 59.14, 69.95, 77.16 and 79.61° assigned to the (110), (200), (220), (311), (222), (400), (331) and (420) lanes marginally shifted towards a lower Bragg's 2θ angle which can be presumed due to synergistic interaction between MoS_2 and CeO_2 [54].

Scanning Electron Microscopy (SEM)

Illustrated in Fig. 2, general morphologies of CeO_2 , MoS_2 and CMS-4 nanocomposite can be observed. The inset images display SEM images under high magnification. CeO_2 nanoparticles can be observed in Fig. 2a. Illustrated in Fig. 2b, pure MoS_2 comprises of large micron spheres that are tightly combined and are flowerlike along the overlapped or coalesced nanosheet structure. Even when two nanosheets are combined, MoS_2 nanosheets are dispersed at the CeO_2 surface. Due to this, it tends to exist in the form of smaller nanosheets (Fig. 2c). The reason for the reduced sheets was large surface area and increase in nucleation sites provided by CeO_2 which possibly results in the decreased aggregation of MoS_2 nanosheets, which is helpful in enhancing the surface-active sites.

Transmission Electron Microscopy (TEM)

TEM with SAED were employed to study the morphology and particle range of CMS-4 nanocomposite. Fig. 3a-c clearly displays the formation of nanocomposite in which nanoparticles (CeO_2) are evenly distributed on the surface of nanosheets (MoS_2). Fig. 3c displays CeO_2 nanoparticles with lateral particle size in the range of 12-22 nm. Well defined fringes with inter planar distance between lattice spacing were calculated to be ~ 0.303 and 0.281 nm corresponding to the (111) and (200) planes of CeO_2 [55]. Another informative view of HR-TEM clear lattice fringe ~ 0.623 nm is ascribed to the (002) plane of MoS_2 nanosheets [56]. The SAED pattern of CMS-4 nanocomposite is displayed in Fig. 3e which exhibits the crystalline nature of the composite. The indicated red dots point measured are SAED d-spacing values which are 0.3203 , 0.2795 , 0.1938 , 0.1674 and 0.1566 nm corresponding to crystalline planes of (111), (200), (220), (311), (222) and (400) CeO_2 and was matched well with XRD pattern of CeO_2 (PDF-2 card no. 00-004-0593). Particle size distribution histogram confirms that the average lateral particle size of CeO_2 nanoparticles were 15.4 nm its standard deviation was found out to be 2.99 (Fig. 3f).

X-ray Photoelectron Spectroscopy (XPS)

XPS was used to study the surface chemical compositions and valence state of $\text{CeO}_2/\text{MoS}_2$ nanocomposite. Fig. 4a shows the survey scan for CMS-4 nanocomposite and peaks for Ce, O, Mo, S, C elements can be observed. XPS scan for individual elements are present in Fig. 4b-e.

Due to the mixed valence state of Ce, many peaks were observed as illustrated in Fig. 4b. Two core XPS level groupings, one $3d_{5/2}$ type 880 to 900 eV, and the other $3d_{3/2}$ set 900 to 920 eV were observed. The binding energy of the XPS 914.5 and 886.5 eV peaks of the Ce^{+4} equals $3d_{3/2}$ and $3d_{5/2}$ respectively [57]. Main XPS peaks of Ce belonged to $3d_{3/2}$ and $3d_{5/2}$ at 903.0 and 883.1 eV, correspondingly. Oxygen peaks in nanocomposite for O 1s can be observed in Fig. 4c. Due to the asymmetry in O 1s region, presences of two types of oxygen species are predicted. Lattice oxygen is attributed to the presence of a strong peak in 530.3 eV and a peak of 527.1 eV to chemisorbed oxygen on the Nanocomposite's [57]. Fig. 4d indicates the reduction of Mo in the synthesis of MoS_2 from Mo as a precursor. The doublet binding energy for $3d_{3/2}$ and $3d_{5/2}$ were 230.5 eV and 227.4 eV respectively. Reduction of Mo from oxidation state of $+6$ to $+4$ was indicated in Mo 3d XPS spectra [58]. In the region of S 2p, two peaks are observed at 161.1 eV and 159.3 eV which corresponded to S $2p_{1/2}$ and S $2p_{3/2}$ respectively (Fig. 4e) [59].

Photocatalytic Activity

Experiments prove that the degradation of dyes (such as MV) was not possible in the absence of photocatalyst obtained under visible light (Fig. 5b). Hence, photodegradation of MV dye was done under visible light using CeO_2 , MoS_2 and $\text{CeO}_2/\text{MoS}_2$ as photocatalysts. In order to monitor the progress of

photodegradation reactions, absorbance of irradiated dye solution is measured (Fig. 5). The previous literatures were compared with the present study as shown in Table S1.

Visible light degradation of MV dye in the presence of photocatalysts, CeO₂ and MoS₂ exhibit low degradation rate as observed in Fig. 6a. The rate of removal after 90 min of irradiation was only 47.37% and 80.8% for CeO₂ and MoS₂, respectively. The CeO₂/MoS₂ nanocomposites sample has more degradation ability than that of pure CeO₂ and MoS₂. The reason for this could be adequate adsorption and enough reaction sites present on the surfaces of the nanocomposites.

The CMS-4 nanocomposite attains the highest photocatalytic activity among the prepared different percentage (2, 4, 6, and 8%) composites, possessing the degradation ratio of 96.25% within 90 min. The photocatalytic efficiency of CMS-4 nanocomposite in degrading MV dye was about 2.03 times and 1.19 times than that of pure CeO₂ and MoS₂ correspondingly. This proves that the loading of MoS₂ on the CeO₂ have a critical effect on the photocatalytic activity. Moreover, it was noted that if the weight percent of MoS₂ in the composite was increased beyond 4 %, noticeable reduction in the photocatalytic activity was observed. It was due to loss of heterogeneity on the catalyst surface due to excess of MoS₂ in the CeO₂/MoS₂ nanocomposite it decreased the absorption of visible light. Whereas the MoS₂ percentage in 300 mg of CeO₂ is as low as 2 %, there were not enough MoS₂ reached on CeO₂. Further, regulation of bandgap and accelerating the mobility of carriers can be done effectively by the 3D/2D heterostructure due to which longer lifespan of the photoexcited electron-hole pairs and more effective separation can be obtained. Control of grain size of nano ranged CeO₂ and its agglomeration was prevented by layering 2D MoS₂ and hence more reactive sites and large surface area was attained. To differentiate the photocatalytic activity of the prepared catalyst, kinetic activity of dye degradation was conducted. The UV-Vis spectrum for a fixed concentration of MV dye with CMS-4 catalyst and varying irradiation time is illustrated in Fig. 5a. The shift of the peak ranging from 584 nm to 580 nm for the maximum absorption for MV was due to the cyclo-reversion and azo group removal. As the irradiation time increased, more MV dye molecules degraded, resulting in the decrease in dye concentration; consequently, the adsorption intensity of the light decreased. The more the dye molecules in the solution more will be the absorption intensity.

As illustrated in Fig. 6b, the MV dye degradation kinetics was followed the following equation,

$$\ln (C_0/C) = -kt.$$

The value of k for CMS-4 nanocomposite (0.0365 min⁻¹) was 13.1 times and 7.2 times more as that of MoS₂ (0.0183 min⁻¹) and CeO₂ (0.00713 min⁻¹) respectively. Thus, CMS-4 will considerably elevate the separation efficacy of the charge carriers, and the MV molecules are almost removed after 90 min under visible light irradiation.

Photocatalytic mechanism of CeO₂/MoS₂

Based on the results of this study, we propose a conceivable photocatalytic mechanism as illustrated in (Fig. 7). The molecules of CeO₂ and MoS₂ get excited instantly during visible light irradiation to yield holes (the characteristic property of photocatalysts) and photogenerated electrons in their respective valence band (VB) and conduction band (CB). The energy gap between conduction band and the valence band for CeO₂ was 2.66 eV, which was higher than that of MoS₂ for which the energy gap was 1.81 eV. The MoS₂ was activated under visible light illumination and the photogenerated electrons are being transferred from the surface of MoS₂ to the surface of CeO₂. The conduction band's electrons (e⁻) generate the ·O₂⁻ radicals along with oxygen (O₂) molecules. The holes (h⁺) in the valence band works with OH⁻ group to generate a hydroxyl radical (·OH). Further reaction of ·O₂⁻ groups in water, leads to the formation of hydroxyl radicals [60]. Oxidization of MV was done by the hydroxyl radicals to form CO₂, H₂O along with other small-sized non-polluting molecules. We believe that CMS-4 nanocomposite possesses extraordinary photocatalytic performance due to the 3D/2D heterojunction structure which encourages the separation and transfer of the electron-hole pairs; based on the results

Statistical Optimization of degradation study

Explanation of regression analysis

In CCD, the experiments were planned randomly to minimize the effect of uncontrolled variables. As illustrated in the Table S2, 2, three independent variables - the amount of photocatalyst as Z1, the concentration of MV dye as Z2, and time for degradation as Z3 was introduced into the 3 levels (low, basal and high) coded as (-1, 0, +1) respectively. Responses of all 20 experiments obtained were unveiled in Table 2. Analysis of variance (ANOVA) was computed using MINITAB17 for finding important effects and interactions (Table S3). 95 % confidence in statistical significance is suggested as per the p-value which was less than 0.05 in the ANOVA. F-test was applied for evaluation of statistical significance within confidence interval of 95% [61, 62]. Data analysis of semi-empirical expression for % of MV removal is presented as:

$$\begin{aligned} \text{\% of MV removal} = & 95.309 + 2.344 Z1 + 1.217 Z2 + 2.531 Z3 - 3.44 \\ & Z1*Z1 - 1.95 Z2*Z2 - 4.94 Z3*Z3 - 0.062 Z1*Z2 - 0.187 Z1*Z3 + 0.570 \\ & Z2*Z3 \end{aligned}$$

Experimental values of degradation percent were compared to the empirical values and plotted (Fig. S1). The outcomes of ANOVA (Table S3) indicate that the significance of the model (p < 0.01) with F- value of 103.853 [61]. The predicted R² of 93.24% was in reasonable agreement with the adjusted R² of 85.72 %

[63]. Yet, the Non-significant lack of fit was good. Lack of fit F-value was 6.69 and this implies that the lack of fit was insignificant concerning the pure error and can be used for further analysis [64, 65]. Henceforth, this analysis allowed the use of a response surface for modelling the design space. All factors exert noteworthy effect on light intensity since all of them have a p-value of less than 0.05. 42.01 was the adequate precision which implies a requisite quadratic model. The maximum MV degradation (96.25 %) of the photocatalyst was 20 mg and the MV dye concentration was 20 mg/L for a time period of 90 min.

Optimization by employing RSM approach

In the next unit RSM was developed in order to increase the critical factors for describing the nature of the responding surface in the experiment, taking into account all remarkable interactions in the CCD. Fig. 8, S8 shows the most appropriate design response surfaces and depicts the MV degradation response percentage of the surface compared to major variables [66-68]. Presented graphs were plotted for a given pair of factors at optimum conditions and other variables were fixed. The relation amongst the variables is indicated by the art of the plots. Fig. 8a, S8a shows the degradation percentage of MV with the amount of photocatalyst (Z1) and the concentration of MV dye (Z2). The enhancement in degradation percentage of MV at a higher dose of the amount of photocatalyst (Z1) was noticed which may attribute to increase in reaction sites. The response surfaces plots Fig. 8b, S8b demonstrated the degradation percentage of MV as a function of the amount of photocatalyst (Z1) and time for degradation (Z3) while their interaction is considered. The percentage removal increased with enhancement with the amount of photocatalyst because of its small particle size and high specific surface area. The suggestively increase in rate of adsorption was observed at higher values. At a lower value of the amount of photocatalyst, due to insufficient reactive sites and a lower ratio of dye molecules to vacant sites, percentage degradation significantly decreased. The effect of concentration of MV dye (Z2) versus time for degradation (Z3) on the degradation percentage with its effect on factors are presented in Fig. 8c, S8c. It was observed that, in spite of increasing the of concentration of MV, its degradation efficiency decreases. The ratio of concentration of solute to unoccupied reactive adsorbent sites is low at lower concentration of dye and dye adsorption is accelerated, thus enhancing dye degradation. On the other hand, saturation of adsorption sites leads to low adsorption yield at high concentrations. Conversely, dye degradation percentage was high at lower initial concentration of dye while degradation was low at higher initial percentage. This indicates that initial concentration is important for adsorption of dyes.

Reusability and stability of CeO₂/MoS₂ composites

Stability and reusability account as critical factors for photocatalysts in real-world applications. The photocatalytic degradation process was repeated five times and the results are presented (Fig. 9a). The motive for this repetitive experiment was to check the activity-stability of the nanocomposites prepared. The photocatalytic activity of CMS-4 does not have any observable change even after five recycles in the

degradation of MV dye solution. Since the catalyst prepared is insoluble in water, the mass loss during the recycling process was insignificant. To notice the stability and reusability, the photocatalyst samples were characterized using XRD before and after the photocatalytic degradation process. It was observed that after the photocatalytic degradation process was completed, the intensity of catalysts remained unchanged as shown in Fig. 9b. Thus, we can infer that 3D/2D heterojunction of CeO₂/MoS₂ owns exceptional photocatalytic recyclability and excellent stability in real-world applications.

Conclusion

3D/2D CeO₂/MoS₂ nanocomposites has been successfully synthesized using the peel extract of *M. oleifera*. The nanocomposites were characterized using various analytical procedures: UV-Visible diffuse reflectance spectroscopy, FT-IR, XRD, XPS, SEM and EDAX, TEM and SAED pattern, Zeta potential and Photoluminescence spectroscopy techniques. The characterization techniques convincingly supported the formation of the CeO₂/MoS₂ nanocomposites, in which CeO₂ nanoparticles are effectively dispersed on MoS₂ nanosheets. The synthesized nanocomposites are verified through degradation of methyl violet dye. Moreover, it is proved that the synthesized nanocomposites are stable and can be reused upto five times. It can be concluded that CeO₂/MeS₂ nanocomposite had brilliant erosion stability after five cycles and good photocatalytic activity. Additionally, optimization was done using RSM and parameters like the amount of photocatalyst, time for degradation and concentration of MV dye were investigated using Central Composite Design of Experiments. Combination of experimental method and statistical predication tool could be an effective method to predict the degradation percentage of pollutants.

Declarations

Conflict of interest

The authors declare that they have no known competing financial interests or personal relationships that could have appeared to influence the work reported in this paper.

References

1. S. J. Varjani, E. Gnansounou, and A. Pandey, Chemosphere 188, 280 (2017).
2. M. A. Ashraf, Environ. Sci. Pollut. Res. 24, 4223 (2017).
3. G. Zhang, X. Zhang, Y. Meng, G. Pan, Z. Ni, and S. Xia, Chem. Eng. J. 392, 123684 (2020).
4. L. A. Thompson and W. S. Darwish, J. Toxicol. 2019, 1 (2019).
5. C.-C. Wang, J.-R. Li, X.-L. Lv, Y.-Q. Zhang, and G. Guo, Energy Environ. Sci. 7, 2831 (2014).
6. I. M. Bulai and E. Venturino, J. Math. Chem. 54, 1387 (2016).
7. S. Zhang, M. Zeng, J. Li, J. Li, J. Xu, and X. Wang, J. Mater. Chem. A 2, 4391 (2014).

8. D. Medeiros de Araújo, P. Cañizares, C. A. Martínez-Huitle, and M. A. Rodrigo, *Electrochem. Commun.* 47, 37 (2014).
9. R. R. Christopher FC, Ponnusamy SK, Ganesan JJ, *IET Nanobiotechnology* 13, 243 (2019).
10. J. Wen, J. Xie, X. Chen, and X. Li, *Appl. Surf. Sci.* 391, 72 (2017).
11. D. Liu, Y. Fernández, O. Ola, S. Mackintosh, M. Maroto-Valer, C. M. A. Parlett, A. F. Lee, and J. C. S. Wu, *Catal. Commun.* 25, 78 (2012).
12. A. Chauhan, M. Sharma, S. Kumar, S. Thirumalai, R. V. Kumar, and R. Vaish, *J. Hazard. Mater.* 381, 120883 (2020).
13. L. W. Humayun M, Raziq F, Khan A, *Green Chem. Lett. Rev.* 11, 86 (2018).
14. Q. Fan, Y. Huang, C. Zhang, J. Liu, L. Piao, Y. Yu, S. Zuo, and B. Li, *Catal. Today* 264, 250 (2016).
15. A. Sirelkhatim, S. Mahmud, A. Seeni, N. H. M. Kaus, L. C. Ann, S. K. M. Bakhori, H. Hasan, and D. Mohamad, *Nano-Micro Lett.* 7, 219 (2015).
16. F.-H. Chu, C.-W. Huang, C.-L. Hsin, C.-W. Wang, S.-Y. Yu, P.-H. Yeh, and W.-W. Wu, *Nanoscale* 4, 1471 (2012).
17. G. Elango and S. M. Roopan, *J. Photochem. Photobiol. B Biol.* 155, 34 (2016).
18. Z. Zhang, M. F. Hossain, and T. Takahashi, *Appl. Catal. B Environ.* 95, 423 (2010).
19. L. Xu and J. Wang, *Environ. Sci. Technol.* 46, 10145 (2012).
20. S. Zhang, P. Gu, R. Ma, C. Luo, T. Wen, G. Zhao, W. Cheng, and X. Wang, *Catal. Today* 335, 65 (2019).
21. S. Usai, S. Obregón, A. I. Becerro, and G. Colón, *J. Phys. Chem. C* 117, 24479 (2013).
22. M. Wu, L. Li, N. Liu, D. Wang, Y. Xue, and L. Tang, *Process Saf. Environ. Prot.* 118, 40 (2018).
23. D. Voiry, M. Salehi, R. Silva, T. Fujita, M. Chen, T. Asefa, V. B. Shenoy, G. Eda, and M. Chhowalla, *Nano Lett.* 13, 6222 (2013).
24. H. Hwang, H. Kim, and J. Cho, *Nano Lett.* 11, 4826 (2011).
25. X. Gan, H. Zhao, and X. Quan, *Biosens. Bioelectron.* 89, 56 (2017).
26. Z. Wang and B. Mi, *Environ. Sci. Technol.* 51, 8229 (2017).
27. L. Cao, R. Wang, D. Wang, L. Xu, and X. Li, *Chem. Phys. Lett.* 612, 285 (2014).
28. Z. Zhou, Y. Lin, P. Zhang, E. Ashalley, M. Shafa, H. Li, J. Wu, and Z. Wang, *Mater. Lett.* 131, 122 (2014).
29. Q. Wang, G. Yun, Y. Bai, N. An, J. Lian, H. Huang, and B. Su, *Appl. Surf. Sci.* 313, 537 (2014).
30. W. Peng and X. Li, *Catal. Commun.* 49, 63 (2014).
31. R. Ma, S. Zhang, T. Wen, P. Gu, L. Li, G. Zhao, F. Niu, Q. Huang, Z. Tang, and X. Wang, *Catal. Today* 335, 20 (2019).
32. V. Lair, A. Ringuedé, P. Vermaut, and S. Griveau, *Phys. Status Solidi* 5, 3492 (2008).
33. K. Kamada, K. Horiguchi, T. Hyodo, and Y. Shimizu, *Cryst. Growth Des.* 11, 1202 (2011).
34. M. Hejazifar, O. Lanaridi, and K. Bica-Schröder, *J. Mol. Liq.* 303, 112264 (2020).

35. T. V. Surendra and S. M. Roopan, *J. Photochem. Photobiol. B Biol.* 161, 122 (2016).
36. A. I. Y. Tok, S. W. Du, F. Y. C. Boey, and W. K. Chong, *Mater. Sci. Eng. A* 466, 223 (2007).
37. A. I. Y. Tok, F. Y. C. Boey, Z. Dong, and X. L. Sun, *J. Mater. Process. Technol.* 190, 217 (2007).
38. N. Wetchakun, S. Chaiwichain, B. Inceesungvorn, K. Pingmuang, S. Phanichphant, A. I. Minett, and J. Chen, *ACS Appl. Mater. Interfaces* 4, 3718 (2012).
39. D. You, B. Pan, F. Jiang, Y. Zhou, and W. Su, *Appl. Surf. Sci.* 363, 154 (2016).
40. Z.-M. Yang, S.-C. Hou, G.-F. Huang, H.-G. Duan, and W.-Q. Huang, *Mater. Lett.* 133, 109 (2014).
41. Y. C. Zhang, M. Lei, K. Huang, C. Liang, Y. J. Wang, S. S. Ding, R. Zhang, D. Y. Fan, H. J. Yang, and Y. G. Wang, *Mater. Lett.* 116, 46 (2014).
42. X. Wang, B. Zhai, M. Yang, W. Han, and X. Shao, *Mater. Lett.* 112, 90 (2013).
43. J. Zhang, B. Wang, C. Li, H. Cui, J. Zhai, and Q. Li, *J. Environ. Sci.* 26, 1936 (2014).
44. Q. Leng, D. Yang, Q. Yang, C. Hu, Y. Kang, M. Wang, and M. Hashim, *Mater. Res. Bull.* 65, 266 (2015).
45. K. R. S. Devi, S. Mathew, R. Rajan, J. Georgekutty, K. Kasinathan, D. Pinheiro, and S. Sugunan, *Appl. Surf. Sci.* 494, 465 (2019).
46. M. Jourshabani, Z. Shariatnia, and A. Badiei, *J. Mater. Sci. Technol.* 34, 1511 (2018).
47. K. M. Garadkar, A. A. Patil, P. P. Hankare, P. A. Chate, D. J. Sathe, and S. D. Delekar, *J. Alloys Compd.* 487, 786 (2009).
48. S. Biswas, M. Bal, S. Behera, T. Sen, and B. Meikap, *Water* 11, 325 (2019).
49. V. Rac, V. Rakić, D. Stošić, V. Pavlović, S. Bosnar, and A. Auroux, *Arab. J. Chem.* 13, 1945 (2020).
50. A. S. Abdulhameed, A. H. Jawad, and A.-T. Mohammad, *Bioresour. Technol.* 293, 122071 (2019).
51. T. V. Surendra, S. M. Roopan, D. Devipriya, M. M. Rahman Khan, and R. Hassanien, *Compos. Part B Eng.* 172, 690 (2019).
52. H. Li, F. Meng, J. Gong, Z. Fan, and R. Qin, *J. Alloys Compd.* 722, 489 (2017).
53. M. Li, D. Wang, J. Li, Z. Pan, H. Ma, Y. Jiang, and Z. Tian, *RSC Adv.* 6, 71534 (2016).
54. X. Liu, F. Meng, B. Yu, and H. Wu, *J. Mater. Sci. Mater. Electron.* 31, 6690 (2020).
55. T. Taniguchi, Y. Sonoda, M. Echikawa, Y. Watanabe, K. Hatakeyama, S. Ida, M. Koinuma, and Y. Matsumoto, *ACS Appl. Mater. Interfaces* 4, 1010 (2012).
56. K. Chang, Z. Mei, T. Wang, Q. Kang, S. Ouyang, and J. Ye, *ACS Nano* 8, 7078 (2014).
57. M. J. Islam, D. A. Reddy, J. Choi, and T. K. Kim, *RSC Adv.* 6, 19341 (2016).
58. T. Lin, J. Wang, L. Guo, and F. Fu, *J. Phys. Chem. C* 119, 13658 (2015).
59. H. Wang, F. Wen, X. Li, X. Gan, Y. Yang, P. Chen, and Y. Zhang, *Sep. Purif. Technol.* 170, 190 (2016).
60. M. Alomar, Y. Liu, W. Chen, and H. Fida, *Appl. Surf. Sci.* 480, 1078 (2019).
61. M. Bilici Baskan and A. Pala, *Desalination* 254, 42 (2010).
62. A.-C.C. Myers RH, Montgomery DC, (2016)
63. J. Jaafari and K. Yaghmaeian, *Desalin. WATER Treat.* 142, 225 (2019).

64. E. Yabalak, Ö. Görmez, and A. M. Gizir, J. Environ. Sci. Heal. Part B 53, 334 (2018).
65. D. Chakraborty, G. Gupta, and B. Kaur, Protein Expr. Purif. 128, 123 (2016).
66. P. Nitnithiphrut, R. Pimsri, and V. Seithtanabutara, Key Eng. Mater. 718, 100 (2016).
67. V. K. Gupta, A. Fakhri, S. Rashidi, A. A. Ibrahim, M. Asif, and S. Agarwal, Mater. Sci. Eng. C 77, 1128 (2017).
68. Y. Wan, X. Liu, P. Liu, L. Zhao, and W. Zou, Sci. Total Environ. 639, 428 (2018).

Tables

Table 1

Composite composition and Symbol

Material	Percentage of MoS ₂	Percentage of CeO ₂	Composite symbol
CeO ₂	0	100	C
MoS ₂	100	0	MS
2% CeO ₂ / MoS ₂	2	98	CMS-2
4% CeO ₂ / MoS ₂	4	96	CMS-4
6% CeO ₂ / MoS ₂	6	94	CMS-6
8% CeO ₂ / MoS ₂	8	92	CMS-8

Table 2

Response surface CCD model optimization experiments

Std Order	Run Order	Pt Type	Blocks	Z1	Z2	Z3	% degradation of MV	
							Experimental	Theoretical
5	1	1	1	-1	-1	1	85.50	84.81
9	2	0	1	0	0	0	96.25	96.62
8	3	1	1	1	1	1	94.70	92.70
3	4	1	1	-1	1	-1	82.47	81.93
11	5	0	1	0	0	0	96.25	96.62
2	6	1	1	1	-1	-1	86.39	85.70
10	7	0	1	0	0	0	96.25	96.62
6	8	1	1	1	-1	1	89.10	89.25
7	9	1	1	-1	1	1	88.21	88.51
1	10	1	1	-1	-1	-1	78.90	80.51
4	11	1	1	1	1	-1	86.57	86.87
12	12	0	1	0	0	0	96.25	96.62
13	13	-1	2	-1	0	0	88.92	88.20
15	14	-1	2	0	-1	0	91.23	90.82
17	15	-1	2	0	0	-1	87.23	86.51
20	16	0	2	0	0	0	96.25	93.99
19	17	0	2	0	0	0	96.25	93.99
14	18	-1	2	1	0	0	90.68	92.89
18	19	-1	2	0	0	1	89.36	91.57
16	20	-1	2	0	1	0	91.34	93.25

Figures

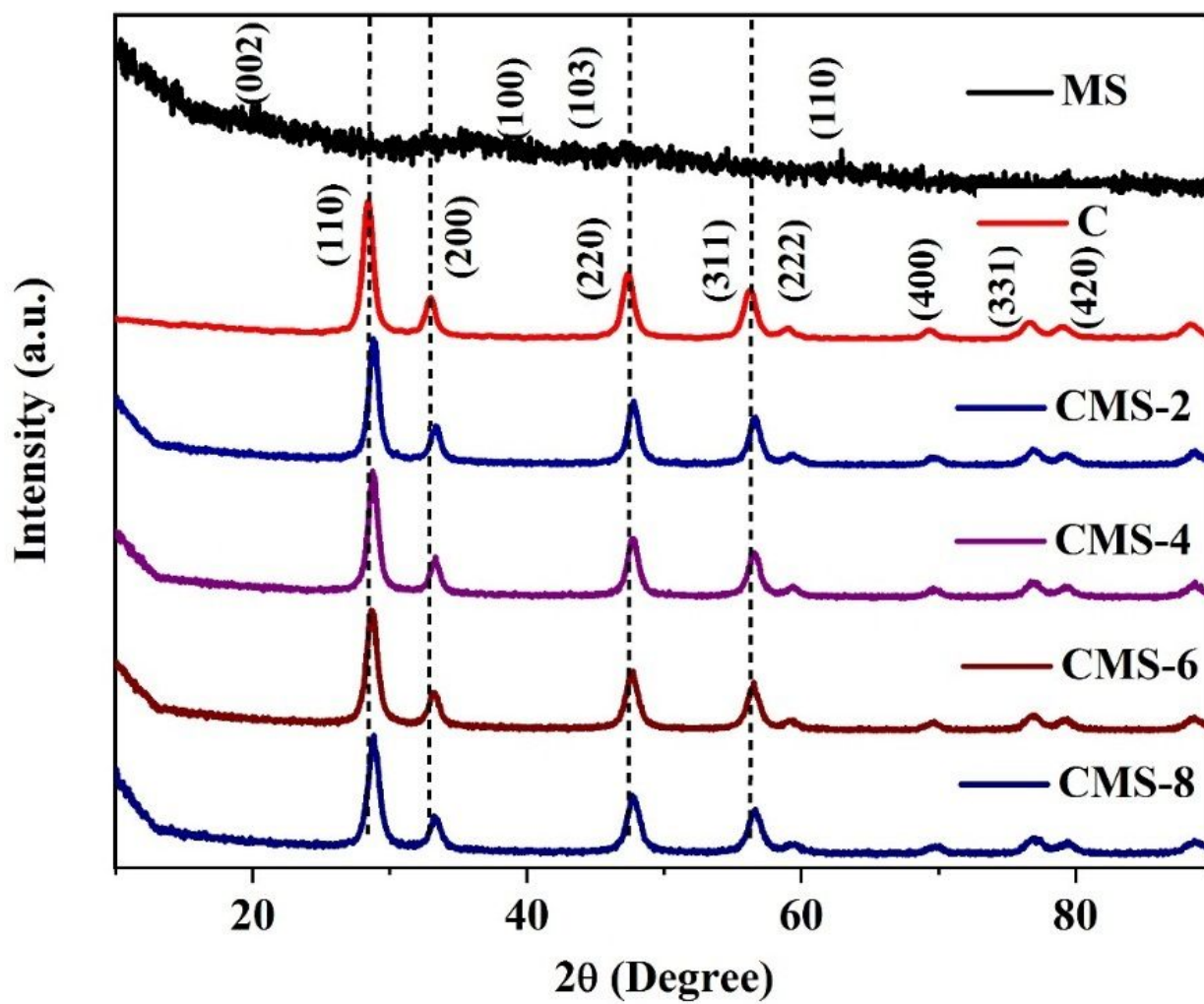


Figure 1

XRD patterns of MoS₂, CeO₂ and CMS (CeO₂/MoS₂ nanocomposites).

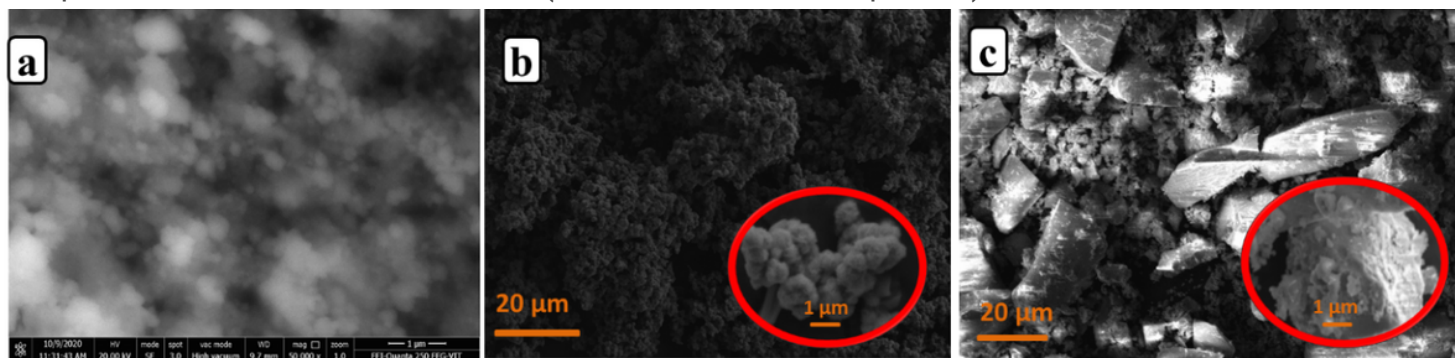


Figure 2

SEM images of a) CeO₂ nanoparticles, b) MoS₂ nanosheets and b) CMS-4.

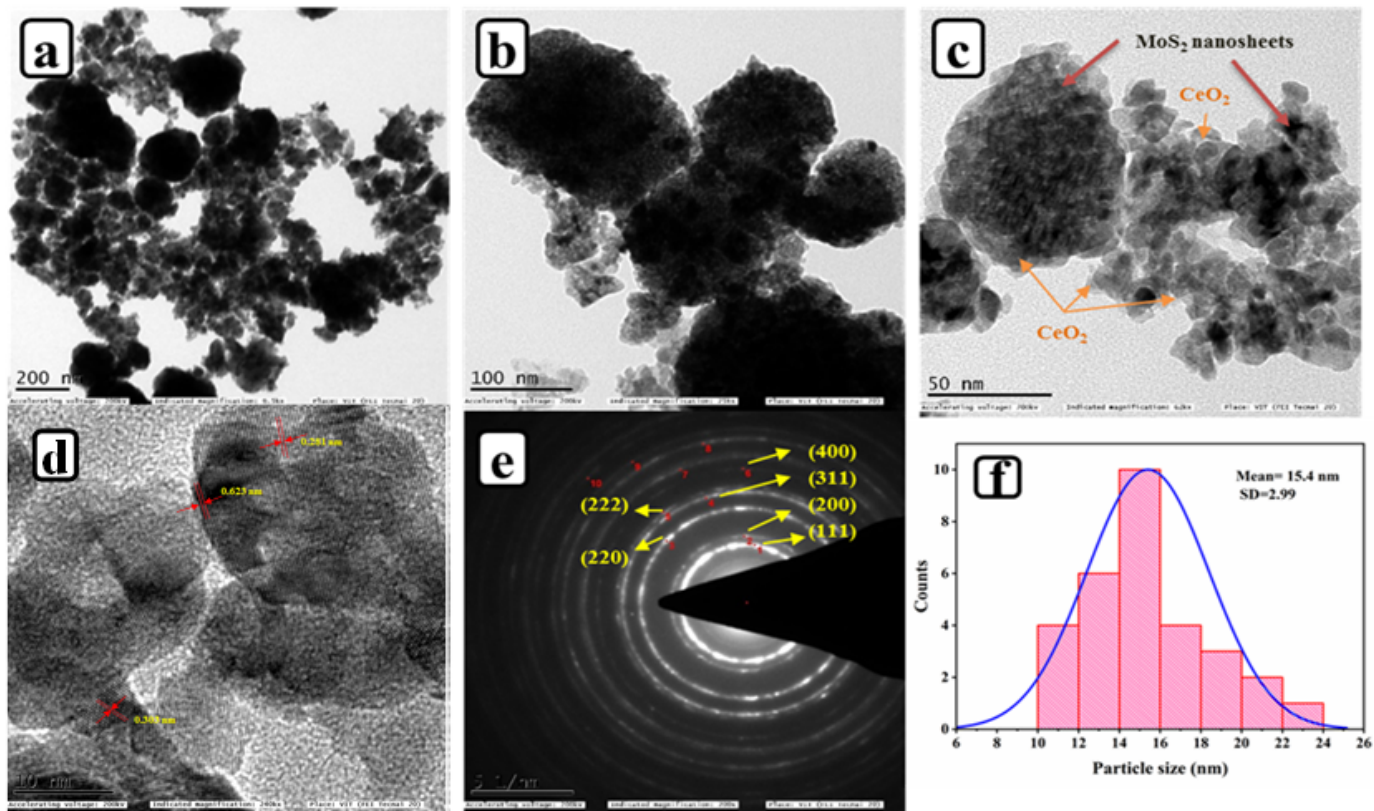


Fig. 3

Figure 3

TEM images of CMS-4 at: a) 200 nm, b) 100 nm, c) 50 nm, d) 10 nm, e) SAED pattern of CMS-4 and f) Particle size distribution histogram.

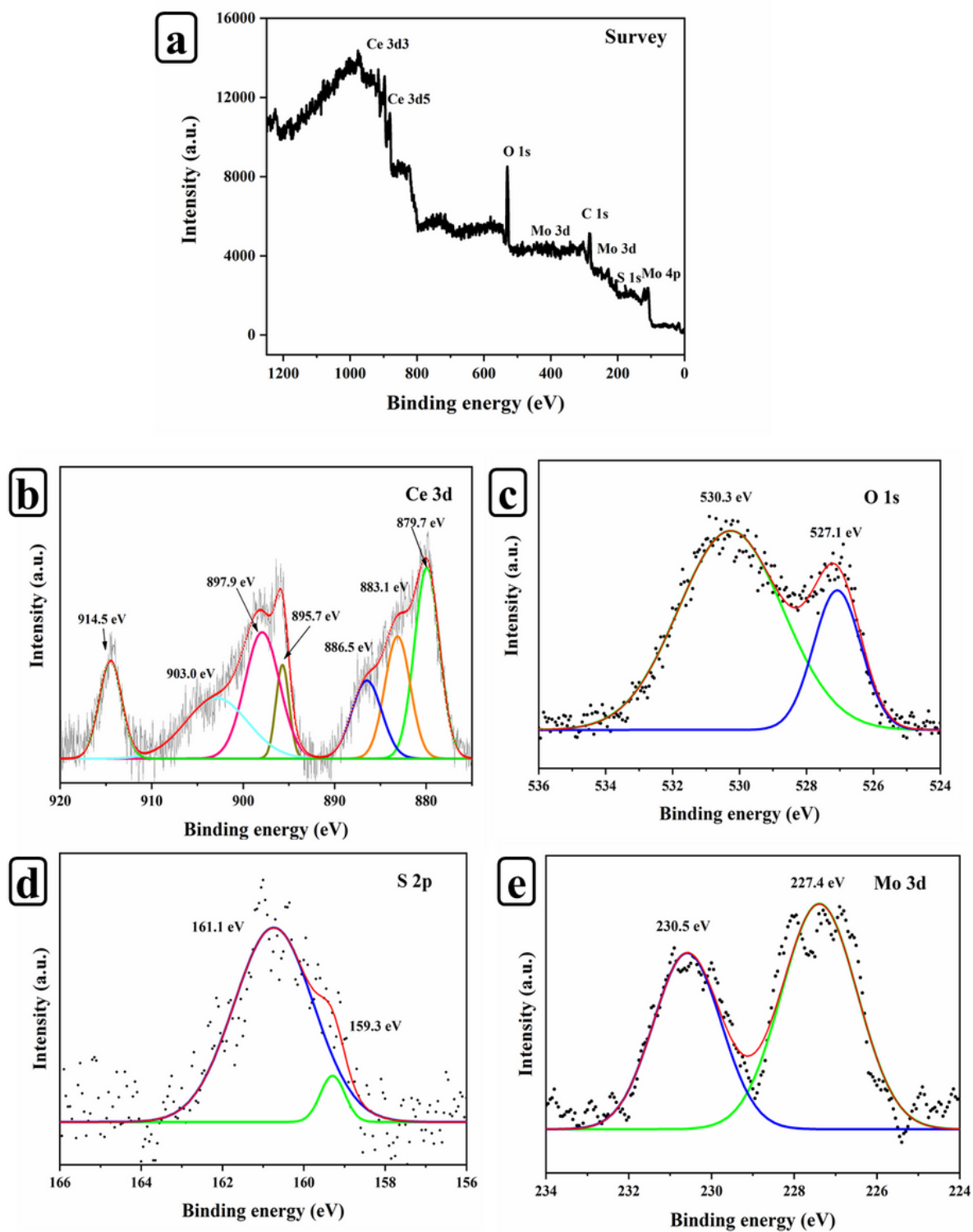


Figure 4

XPS spectra of CMS-4 nanocomposite a) Survey scan, b) Ce 3d, c) O 1s and d) Mo 3d.

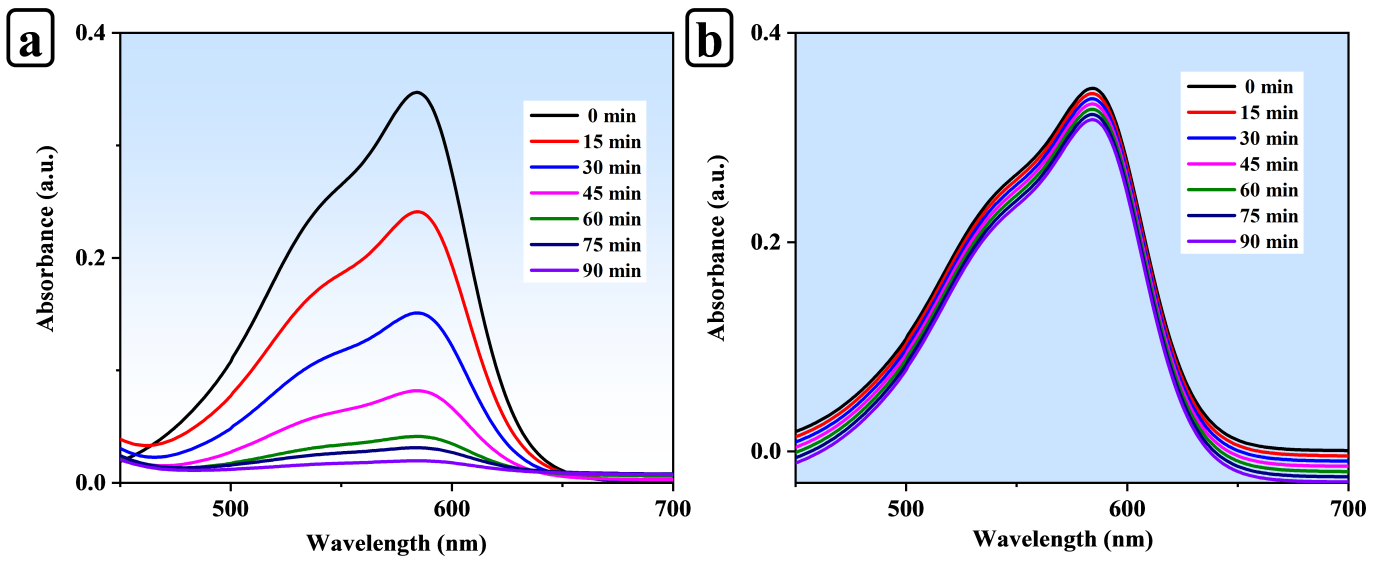


Figure 5

UV absorption spectrum of MV degradation under visible light a) With catalyst and b) Without catalyst.

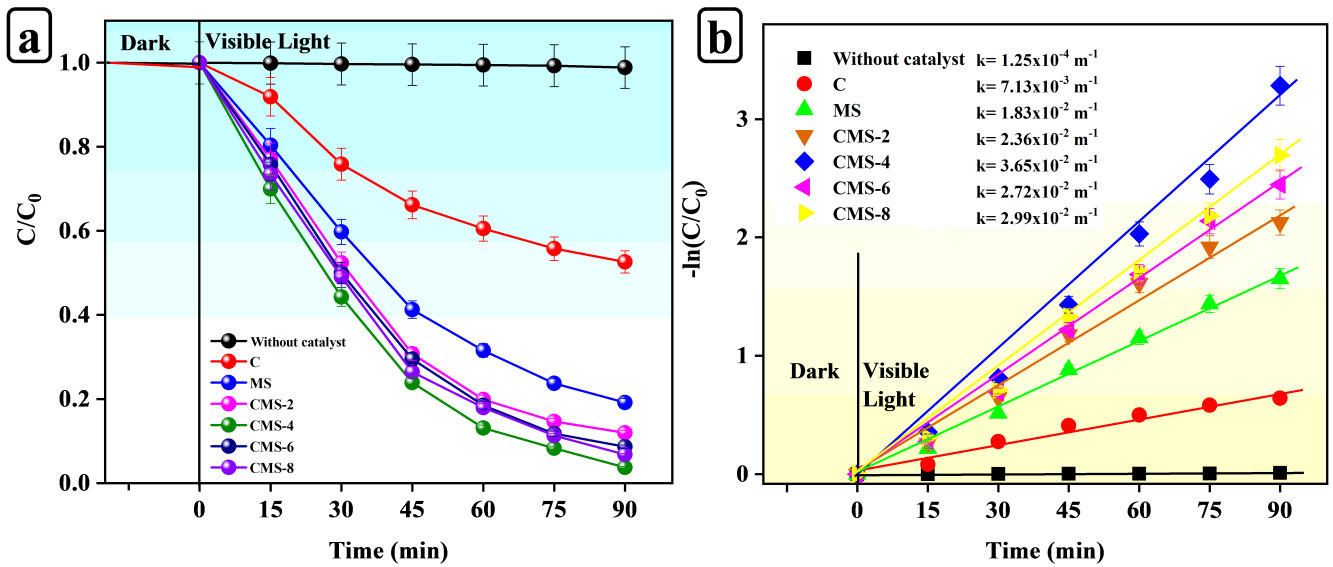


Figure 6

MV degradation under visible light a) Degradation efficiency and b) kinetics plot.

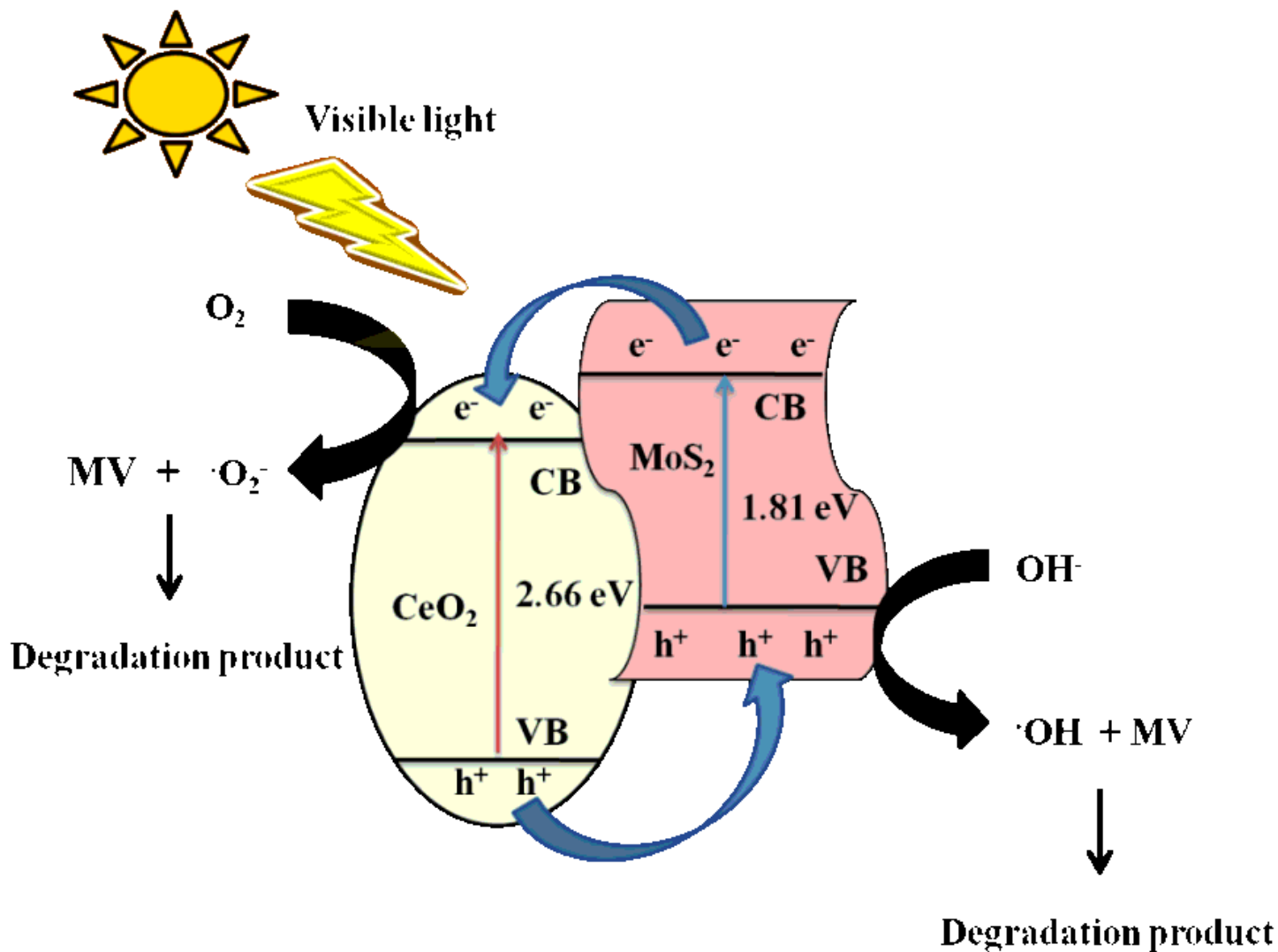


Figure 7

Photocatalytic mechanism of CMS-4 nanocomposite sample.

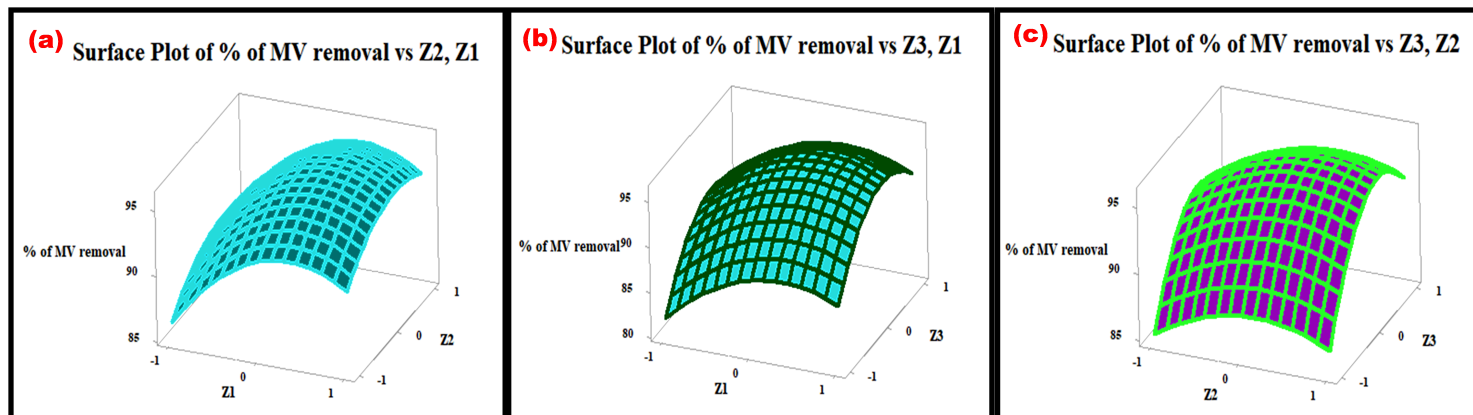


Figure 8

Response surface graph as a function of (a) amount of photocatalyst (Z1) and concentration of MV dye (Z2), (b) amount of photocatalyst (Z1) and time for degradation (Z3), (c) MV dye (Z2) and time for degradation (Z3).

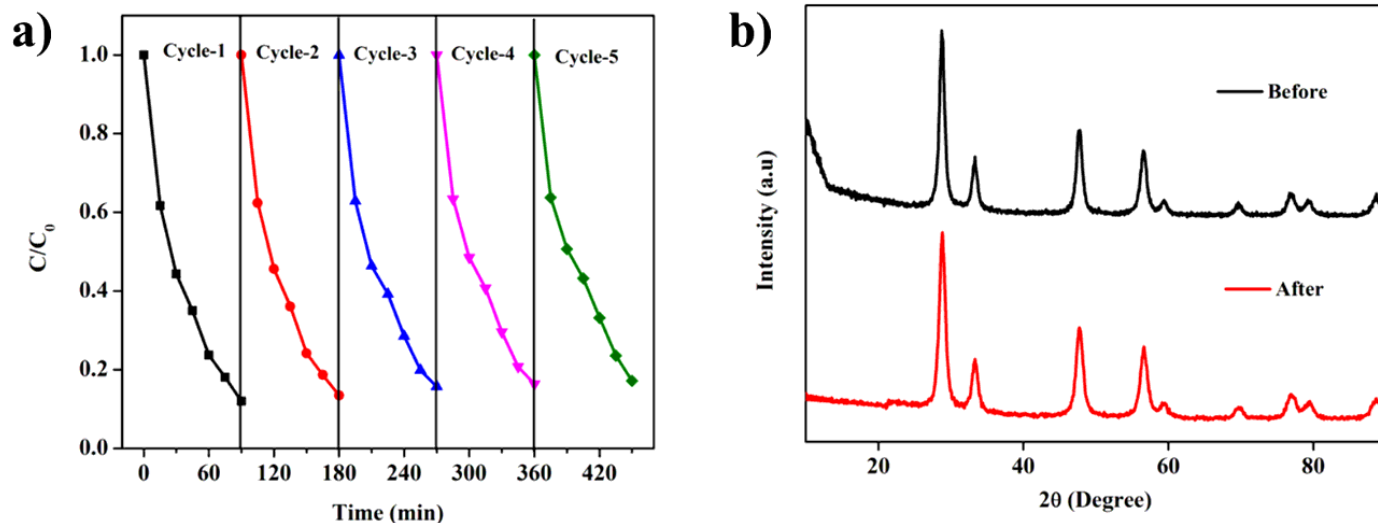


Figure 9

a) Reusability and b) stability.

Supplementary Files

This is a list of supplementary files associated with this preprint. Click to download.

- [SupplementaryInformation.docx](#)